AIMS Mathematics, 11(11): 37764–37794.
DOI: 10.3934/math.20261460
Received: 18 July 2026
Revised: 22 October 2026
Accepted: 28 October 2026
Published: 13 November 2026

https://www.aimspress.com/journal/Math

Research article

Analytical and numerical analysis of a time-dependent mixed integral equation with a hypergeometric kernel

Jihan Alahmadi[1], **M. A. Abdou**[2,*] **and M. Mahmoud Ismail**[3]

[1] Department of Mathematics, College of Science and Humanities in Al-Kharj, Prince Sattam Bin Abdulaziz University, Al-Kharj 11942, Saudi Arabia
[2] Department of Mathematics, Faculty of Education, Alexandria University, Alexandria 21511, Egypt
[3] Department of Mathematics, Faculty of Science, Alexandria University, Baghdad St., Moharam Bek, 21568 Alexandria, Egypt

* **Correspondence:** Email: abdella_777@alexu.edu.eg.

Abstract: We study a class of time-dependent mixed generalized Volterra–Fredholm integral equations with hypergeometric Banach space spatial kernel $X = C([0, T]; L^2(-1, 1))$. The formulation proposed involves several important singular kernels; as special cases, consider the logarithmic, Carleman, and complete elliptic kernels. The Banach fixed-point theorem is used to establish adequate conditions for existence and uniqueness under appropriate assumptions on the spatial kernel and the temporal memory function, with the contraction constraint $BM_G < \mu$. A quadrature-based Nyström-type discretization is employed for the numerical treatment of the spatial integral operator. Numerical studies are performed for the logarithmic, Carleman, complete elliptic, and general hypergeometric cases at selected times to investigate the effects of temporal memory, kernel singularity, and the kernel parameters on the computed solution. The numerical accuracy and convergence behavior are also examined through appropriate error and refinement measures.

Keywords: mixed Volterra–Fredholm integral equation; hypergeometric kernel; $C([0, T]; L^2(-1, 1))$; existence and uniqueness; time-dependent operator coupling; numerical analysis
Mathematics Subject Classification: 45B05, 45D05, 65R20

1. Introduction

Mixed Volterra–Fredholm integral equations naturally arise in problems where temporal memory is combined with non-local spatial interactions. In this paper, the spatial operator is constructed using a generalized hypergeometric kernel, from which several important singular kernels are obtained through parameter selections. The main motivation of the present work is to study these kernels in the same

time-dependent mixed formulation, so that the influence of the Volterra memory term can be studied consistently with the analytical properties of the corresponding Fredholm operator. This formulation provides a common framework to study the interaction of temporal memory and various spatial singular operators.

More specifically, Fredholm integral equations describe nonlocal spatial coupling in boundary-value and potential-type problems, including contact, transport, and scattering applications. Volterra integral equations model causal dependence on earlier states, as encountered in hereditary and time-dependent processes. Mixed Volterra–Fredholm formulations combine spatial interactions with temporal memory.

Singular integral equations (SIEs) are one of the most important classes of functional equations because of their wide applications in different sciences such as quantum physics [1], fluid dynamics [2], laser theory [3], electromagnetic scattering [4], heat transfer [4], and mathematical physics [5]. Recent years have witnessed significant advances in the numerical treatment of singular and hypersingular integral equations. Sharif et al. [6] used a numerical technique to solve a nonlinear integro-differential equation with a continuous kernel. Jan [7] used the product Nyström method for solving a mixed integral equation with a singular kernel. Abdou et al. [8] used an orthogonal polynomial method to discuss the numerical solution of a Volterra–Fredholm integral equation (V–FIE) with a discontinuous kernel in position and a continuous kernel in time.

Jan [9] used a collocation method based on orthogonal polynomials to solve a mixed integral equation with a discontinuous kernel in position and a continuous kernel in time. Mosa et al. [10] numerically solved a nonlinear mixed Volterra–Fredholm integral equation of the second kind with a phase-lag term. Mamatova et al. [11] developed a hybrid method combining the homotopy perturbation method and the Gaussian elimination method as a semi-analytical method for solving systems of Cauchy-type singular integral equations of the first kind with constant coefficients. Finally, Sahu et al. [12] proposed a residual-based Galerkin method for the solution of systems of Cauchy-type singular integral equations with unbounded endpoint conditions. For the general theory and numerical treatment of integral equations, including singular kernels, projection methods, and quadrature-based discretizations, we also refer to the classical works of Kress and Atkinson [13, 14]. Standard polynomial approximation techniques and their spectral properties are discussed by Trefethen [15]. More recently, Jan [16] studied a phase-lag mixed integral equation with a generalized symmetric potential kernel, while Nave [17] proposed a modified semi-analytical approach based on the homotopy analysis method for systems of ordinary differential equations. These references provide broader analytical and numerical background relevant to the methods and related formulations considered in the present work.

For Fredholm equations, frequently used numerical approaches include quadrature-based methods, collocation, and Galerkin projection. For Volterra equations, time-ordered quadrature and collocation account for the causal integration interval. In mixed formulations, the discretizations of the spatial and temporal operators must be distinguished, while singular spatial kernels require suitable treatment within the quadrature rule.

Although the above studies provide valuable analytical and numerical methods for several classes of integral equations, most of them deal with a particular kernel or a specific mixed formulation. Hence, the effect of temporal memory on different spatial singular operators is generally studied separately. However, a comparative examination of the logarithmic, Carleman, and complete elliptic specializations of the same generalized hypergeometric kernel within one mixed formulation remains

of interest. Also, the influence of the time-dependent coefficient coupling the Volterra memory term with the spatial Fredholm operator requires more analytical and numerical studies.

Compared with studies that treat a particular spatial kernel or a specific mixed integral equation separately, the present formulation allows several explicitly identified singular kernels to be examined within the same time-dependent Volterra–Fredholm framework. This makes it possible to investigate the effect of the same temporal memory term on different spatial operators while retaining the particular analytical assumptions required by each kernel. The resulting framework therefore provides a direct basis for comparing the influence of kernel type and temporal memory within a common mathematical model.

These observations motivate the present paper where a class of time-dependent mixed Volterra-Fredholm integral equations is considered in the product space $X = C([0, T]; L^2(-1, 1))$. The spatial part of the equation is given by a generalized hypergeometric kernel, from which many important singular kernels can be obtained as special cases. This representation allows studying these kernels in a unique mathematical framework and studying the interaction between the temporal Volterra memory term and the spatial Fredholm operator. The novelty of the present work does not lie in the use of standard fixed-point or approximation techniques per se. In particular, the Banach fixed-point argument, successive-approximation estimates, and perturbation bounds are supporting analytical results and are not presented as new theoretical methods. For comparison, Jan [7] examined a singular mixed equation using a product Nyström method, Abdou et al. [8] studied a Volterra–Fredholm equation with a discontinuous spatial kernel using orthogonal polynomials, and Jan [16] considered a phase-lag mixed equation with a generalized symmetric potential kernel. The specific contribution here is the explicit treatment of the logarithmic, Carleman, and complete elliptic specializations of one hypergeometric spatial kernel within a common mixed formulation, and their comparative numerical examination through the corresponding separated spatial equations under the same prescribed time-dependent coefficient. This is a contribution in the scope of the formulation and comparison, rather than a claim of a new fixed-point principle or a new numerical algorithm.

The main contributions of this paper can be summarized as follows:

- We derive a time-dependent mixed Volterra–Fredholm integral equation in the product space $X = C([0, T]; L^2(-1, 1))$, with a spatial operator generated by a generalized hypergeometric kernel.
- The logarithmic, Carleman, complete elliptic, and harmonic kernels are derived in a common operator representation that allows studying their analytical and numerical properties in a unified setting.
- Sufficient conditions for the existence and uniqueness of the solution are established. The integral operator is proved to be bounded and continuous, and the corresponding fixed-point mapping is contractive.
- The separation of variables technique reduces the original mixed equation to a hypergeometric Fredholm integral equation with an explicit time-dependent coupling coefficient. This coefficient describes how the temporal memory of the system is linked to the spatial singular operator.
- Numerical computations are performed for representative kernel classes in order to determine how the time-dependent coupling changes the solution at early, intermediate, and late times.

To obtain numerical solutions, a quadrature-based spatial discretization is employed for the Fredholm integral operator. The integral term is approximated by a weighted discrete sum over

the spatial mesh, leading to a linear algebraic system for the unknown nodal values. Numerical experiments are then used to study the behavior of the hypergeometric kernel and its associated special cases at different times.

On this basis, we consider the following mixed integral equation of the second kind, in which the Volterra component accounts for temporal memory and the Fredholm component describes the nonlocal spatial interaction:

$$\begin{cases} \mu\Phi(x,t) - \displaystyle\int_0^t G(t,\tau) \int_{-1}^1 K(x,\xi)\Phi(\xi,\tau)\, d\xi\, d\tau = f(x,t), \\ K(\xi,x) = \dfrac{1}{(\xi^2+x^2)^p} F\left(\dfrac{p}{2}, \dfrac{p+1}{2}, \dfrac{q}{2}; \dfrac{4\xi^2x^2}{(\xi^2+x^2)^2}\right), \\ 0 < 2p < q < 2p+2, \qquad |x| \le 1, \qquad 0 \le t \le T < 1, \qquad 0 < \mu < \infty. \end{cases} \tag{1.1}$$

We impose the dynamical conditions:

$$\int_{-1}^1 \Phi(\xi,t)\, d\xi = p(t), \qquad \int_{-1}^1 \xi\Phi(\xi,t)\, d\xi = M(t). \tag{1.2}$$

Here, $F(a,b;c;z) = {}_2F_1(a,b;c;z)$ denotes the Gauss hypergeometric function.

In applied sciences, such as elasticity, fluid mechanics, and solid-state physics, the second condition, which concerns pressure and torque, is crucial for proving the existence of a unique solution. However, in nuclear physics or astrophysics, these two conditions become

$$\Phi(-1,t) = \Phi(1,t) = 0, \qquad 0 \le t \le T < 1. \tag{1.3}$$

Many different methods are used to solve the integral equation (1.1), particularly when $\mu = 0$ and when the kernel takes a logarithmic form, a Carleman form, or a Cauchy form; see [18–20] for the indicated kernel types.

The remainder of this paper is organized as follows. In Section 2, some important special cases, such as the logarithmic kernel, the Carleman kernel, and other related cases, are derived from the hypergeometric kernel. Moreover, the physical meaning of the mixed integral equation is explained. In Section 3, the fundamental conditions required to ensure the existence of a unique solution are established. In Section 4, it is proved that the integral operator maps the considered function space into itself. It is also shown that this operator is continuous and satisfies a contraction condition. By applying Banach's fixed-point theorem, the existence of a unique solution is obtained. In Section 5, the convergence of the solution is investigated. In Section 6, error and stability analyses are presented. In Section 7, the method of separation of variables is used, and the benefits of this separation are discussed. Finally, in Section 8, the solution of the Fredholm integral equation for kernels derived from the hypergeometric kernel and its relationship with time are discussed; the effect of the time operator on the spatial integral operator is explained clearly at three times $t = 0.01, 0.4, 0.9$; moreover, the resulting error in each case is calculated.

Nomenclature

Symbol	Description
x, ξ, y	Spatial variables in $[-1, 1]$.
t, τ, T	Current time, history time, and final time.
Φ, f, μ	Unknown density, prescribed source, and positive model parameter.
$p, q, {}_2F_1$	Hypergeometric-kernel parameters and Gauss hypergeometric function.
G, K	Temporal memory kernel and spatial Fredholm kernel.
$\mathcal{S}, L$	Spatial Fredholm and mixed Volterra–Fredholm operators.
H, X	$L^2(-1, 1)$ and $C([0, T]; H)$, respectively.
A, B, M_G	Temporal-kernel bound, spatial-kernel bound, and time-integral bound.
$P(t), \mathcal{M}(t)$	Prescribed force and moment, when applicable.
$N, M_f, \lambda(t)$	Time factors and coupling coefficient in the conditional separation.
κ	Contraction factor BM_G/μ.
Φ_m, R_m, H_m	Approximate solution, error, and residual.
$E_i, \nu_i, \theta_i, \lambda_i$	Elastic parameters and coefficients in the illustrative contact model.
γ, β, f_i	Rigid displacement, tilt, and surface profiles.

2. Special cases of the hypergeometric kernel and the physical interpretation

In this section, we highlight some important special cases that play a significant role in explaining several physical phenomena. A simplified explanation and analytical commentary are presented for each case by assigning particular values to the parameters p and q of the hypergeometric kernel. Furthermore, the physical interpretation of the mixed integral equation is discussed at the end of this section.

2.1. Inferred special cases and analytical commentary

Several important kernels can be obtained as special cases of the hypergeometric kernel by choosing suitable values of the parameters p and q, using standard identities of the Gauss hypergeometric function and its relation to the complete elliptic integral [21]. These cases are presented as follows:

(1) The logarithmic kernel.
For $p = 1$ and $q = 3$, the hypergeometric kernel reduces to the logarithmic kernel

$$K(\xi, x) = \frac{1}{2\xi x} \ln \left| \frac{\xi + x}{\xi - x} \right|. \tag{2.1}$$

(2) The Carleman kernel.
For $0 < p < 1$ and $q = p + 1$, the hypergeometric kernel reduces to the Carleman kernel

$$K(\xi, x) = |\xi + x|^{-p} |\xi - x|^{-p}. \tag{2.2}$$

(3) The complete elliptic kernel.
For $p = \frac{1}{2}$ and $q = 2$, the hypergeometric kernel reduces to the complete elliptic kernel

$$K(\xi, x) = \frac{2}{\pi(\xi + x)} \mathcal{K}\left(\frac{2\sqrt{\xi x}}{\xi + x}\right), \tag{2.3}$$

where $\mathcal{K}(\cdot)$ denotes the complete elliptic integral of the first kind.

(4) General hypergeometric case.

In addition to the explicitly identified logarithmic, Carleman, and complete elliptic specializations, the general hypergeometric kernel in Eq (1.1) can also be investigated directly for admissible parameter values satisfying

$$0 < 2p < q < 2p + 2.$$

In this case, no additional closed-form specialization is assumed.

2.2. The physical interpretation of the mixed integral equation

As an illustrative contact-mechanics analogue, Eq (1.1) may be represented in the following form, without claiming a derivation from governing elasticity equations:

$$\begin{aligned} &(\lambda_1 + \lambda_2)\Phi(x,t) - (\theta_1 + \theta_2) \int_0^t G(t,\tau) \int_{-1}^1 K(\xi, x)\Phi(\xi,\tau)\, d\xi\, d\tau \\ =&\pi \left[\gamma(t) + \beta(t)x - f_1(x) - f_2(x)\right], \qquad |x| \le 1, \;\; 0 \le t \le T < 1. \end{aligned} \tag{2.4}$$

Equation (2.4) is regarded here as a formal contact-mechanics analogue involving two surfaces associated with elastic materials characterized by (E_i, ν_i), $i = 1, 2$, over the interval $[-1, 1]$. The functions $f_i(x)$, $i = 1, 2$, describe the corresponding surfaces.

For this illustrative analogy, the following assumptions are introduced without deriving them from a governing physical model. If the upper surface is compressed by a variable force $p(t)$, with an eccentric displacement and a moment $M(t)$, then the rigid displacements $\gamma(t)$, $\beta(t) \in C[0, T]$, $T < 1$, are taken into account. The absence of body forces is also assumed. Moreover, the frictional forces in the contact region between the two surfaces are assumed to be sufficiently small and therefore negligible. The corresponding mathematical unknown is a density function, $\Phi(x, t)$, $x \in [-1, 1]$, $t \in [0, T]$. Here, $\theta_i = \frac{1-\nu_i^2}{\pi E_i}$, $i = 1, 2$, where ν_i and E_i denote Poisson's ratio and Young's modulus, respectively, for the ith elastic material. The continuous function $G(t, \tau) \in C([0, T] \times [0, T])$ represents the temporal kernel of the Volterra integral term and parametrizes the prescribed memory dependence in the model. On the other hand, $K(\xi, x)$ is the kernel of the Fredholm integral term, while ${}_2F_1(a, b; c; z)$ denotes the Gauss hypergeometric function.

No constitutive contact law, identification of physical parameters from measured data, or validation against experiments is carried out. Accordingly, this interpretation illustrates possible meanings of the mathematical variables and is not presented as an established physical model or a validated prediction of contact behavior.

The main objective is to obtain the general solution for the unknown density function $\Phi \in C([0, T]; L^2(-1, 1))$, for certain forms of $\gamma(t)$ and $\beta(t)$ in the class $C[0, T]$, $0 \le t \le T < 1$.

3. Integral operator and its boundary conditions

In order to discuss the properties of the mixed integral equation (1.1) and obtain its solution in the space $X = C([0, T]; L^2(-1, 1))$, we write it in the following integral operator form:

$$\mu\Phi(x, t) = f(x, t) + (L\Phi)(x, t). \tag{3.1}$$

The integral operator equation (3.1) may be written as

$$(\mu I - L)\Phi = f, \tag{3.2}$$

where I denotes the identity operator, and

$$(L\Phi)(x, t) = \int_0^t \int_{-1}^1 G(t, \tau)K(x, y)\Phi(y, \tau)\, dy\, d\tau. \tag{3.3}$$

In order to guarantee existence and uniqueness under the stated contraction argument, we impose the following sufficient assumptions, which are not claimed to be necessary:

(1) The function $G(t, \tau)$ is positive and continuous on $[0, T] \times [0, T]$, where $0 \le \tau \le t \le T < 1$, and satisfies

$$|G(t, \tau)| \le A, \qquad A > 0. \tag{3.4}$$

Moreover, assume that

$$M_G = \sup_{0\le t\le T} \int_0^t |G(t, \tau)|\, d\tau < \infty. \tag{3.5}$$

Since $|G(t, \tau)| \le A$, it follows that

$$M_G \le AT.$$

(2) The kernel $K(x, y)$ satisfies the square-integrability condition

$$\left(\int_{-1}^1 \int_{-1}^1 K^2(x, y)\, dx\, dy\right)^{1/2} = B < \infty, \tag{3.6}$$

where B is a positive constant.

The Hilbert–Schmidt assumption must be verified for each kernel. For the Carleman specialization $K(x, y) = |x^2 - y^2|^{-p}$, it holds on $(-1, 1)^2$ for $0 < p < 1/2$; thus, both tested cases $p = 0.01$ and $p = 0.4$ satisfy it. For the general hypergeometric examples $(p, q) = (1/6, 3/2)$ and $(p, q) = (0.4, 2)$, the Gauss hypergeometric factor is bounded on $0 \le z \le 1$ because $q > 2p + 1$. Consequently, $|K(x, y)| \le C(x^2 + y^2)^{-p}$, and $p < 1/2$ ensures square integrability near the origin.

In contrast, the complete elliptic specialization $(p, q) = (1/2, 2)$ and the unregularized logarithmic specialization $(p, q) = (1, 3)$ do not satisfy the full-domain Hilbert–Schmidt assumption. Indeed, in the positive quadrant the hypergeometric factor is at least one, and hence $K(x, y)^2 \ge (x^2 + y^2)^{-2p}$; the latter is not locally integrable at the origin when $p \ge 1/2$. Accordingly, the existence, uniqueness, and stability conclusions based on Eq (3.6) are asserted only for kernels satisfying that assumption. The complete elliptic and full-domain logarithmic examples are not covered by this particular theorem. For the logarithmic numerical example, the kernel restricted to $D_\delta = [-1, -\delta] \cup [\delta, 1]$, $\delta = 0.1$, is square integrable on D_δ^2; this is a regularized-domain statement and does not imply the full-domain Hilbert–Schmidt condition.

(3) The given function f belongs to

$$X = C([0,T]; L^2(-1,1)),$$

and satisfies

$$\|f\|_X = \sup_{0\le t\le T}\left(\int_{-1}^{1} |f(x,t)|^2\,dx\right)^{1/2} < \infty. \tag{3.7}$$

(4) The unknown density function Φ belongs to

$$X = C([0,T]; L^2(-1,1)),$$

and satisfies

$$\|\Phi\|_X = \sup_{0\le t\le T}\left(\int_{-1}^{1} |\Phi(x,t)|^2\,dx\right)^{1/2} < \infty. \tag{3.8}$$

4. Some properties of the integral operator

In this section, we discuss some properties of the integral operator defined in (3.3) through the following two lemmas. Let $X = C([0,T]; L_2(-1,1))$.

Lemma 4.1. The integral operator L, defined by Eq (3.3), maps the space X into itself under assumptions (1)–(4).

Proof. Let $\Phi \in X$. By the Hilbert–Schmidt assumption (3.6), the spatial operator $(\mathcal{S}u)(x) = \int_{-1}^{1} K(x,y)u(y)\,dy$ is well-defined and bounded on $L^2(-1,1)$ by the Cauchy–Schwarz inequality, with $\|\mathcal{S}u\|_{L^2(-1,1)} \le B\|u\|_{L^2(-1,1)}$. Consequently, the temporal integral defining $L\Phi$ is a well-defined $L^2(-1,1)$-valued Bochner integral, since its integrand is strongly measurable and bounded in norm by $AB\|\Phi\|_X$. For each $t \in [0,T]$, using the Hilbert–Schmidt estimate for the spatial integral operator, we obtain

$$\begin{aligned}
\|(L\Phi)(\cdot,t)\|_{L^2(-1,1)} &= \left\| \int_0^t G(t,\tau) \int_{-1}^{1} K(\cdot,y)\Phi(y,\tau)\,dy\,d\tau \right\|_{L^2(-1,1)} \\
&\le \int_0^t |G(t,\tau)| \left\| \int_{-1}^{1} K(\cdot,y)\Phi(y,\tau)\,dy \right\|_{L^2(-1,1)} d\tau \\
&\le B\int_0^t |G(t,\tau)| \|\Phi(\cdot,\tau)\|_{L^2(-1,1)}\,d\tau \\
&\le BM_G\|\Phi\|_X.
\end{aligned} \tag{4.1}$$

Taking the supremum over $t \in [0,T]$, we obtain

$$\|L\Phi\|_X \le BM_G\|\Phi\|_X. \tag{4.2}$$

To justify continuity in time, let $t_m \to t$ in $[0,T]$. Writing

$$(L\Phi)(\cdot,t_m) = \int_0^T \chi_{[0,t_m]}(\tau)G(t_m,\tau)\mathcal{S}\Phi(\cdot,\tau)\,d\tau,$$

we see that the integrands converge in $L^2(-1,1)$ for almost every $\tau \in [0,T]$ by continuity of G. Their norms are bounded by $AB\|\Phi\|_X$, an integrable dominating function on $[0,T]$. The Bochner dominated convergence theorem therefore implies continuity of $t \mapsto (L\Phi)(\cdot,t)$ in $L^2(-1,1)$. Hence,

$$L\Phi \in C([0,T]; L^2(-1,1)) = X.$$

Moreover, from Eq (4.2),

$$\|L\| \leq BM_G.$$

Hence, L is a bounded operator on X.

Consider now the fixed-point operator

$$\mathcal{T}\Phi = \frac{1}{\mu}(f + L\Phi).$$

Assume that

$$BM_G < \mu. \tag{4.3}$$

Define

$$r = \frac{\|f\|_X}{\mu - BM_G}. \tag{4.4}$$

Then, for every $\Phi \in B_r$,

$$\begin{aligned} \|\mathcal{T}\Phi\|_X &\leq \frac{1}{\mu}\left(\|f\|_X + \|L\Phi\|_X\right) \\ &\leq \frac{1}{\mu}\left(\|f\|_X + BM_G r\right) = r. \end{aligned}$$

Thus, $\mathcal{T}$ maps the closed ball $B_r \subset X$ into itself.

If $f = 0$, then $r = 0$ and $B_r = \{0\}$; in this case $\mathcal{T}0 = 0$, so the invariant-ball argument remains valid without requiring a positive radius.

Since $M_G \leq AT$, the stronger condition

$$ATB < \mu$$

is also sufficient for (4.3).

Lemma 4.2. If assumptions (1)–(4) are fulfilled, then the operator $\mathcal{T}\Phi = (f + L\Phi)/\mu$ is continuous and contractive in the Banach space X, provided that $BM_G < \mu$.

Proof. Let $\Phi_1(x,t)$ and $\Phi_2(x,t)$ be two elements of X. Then, from the definition of $\mathcal{T}$, we have

$$\mathcal{T}\Phi_1 - \mathcal{T}\Phi_2 = \frac{1}{\mu}L(\Phi_1 - \Phi_2).$$

Using the same estimate as in Lemma 4.1, we obtain

$$\|L(\Phi_1 - \Phi_2)\|_X \leq BM_G\|\Phi_1 - \Phi_2\|_X. \tag{4.5}$$

Hence,

$$\|\mathcal{T}\Phi_1 - \mathcal{T}\Phi_2\|_X \leq \frac{BM_G}{\mu}\|\Phi_1 - \Phi_2\|_X. \tag{4.6}$$

Since $BM_G < \mu$, we have

$$\frac{BM_G}{\mu} < 1.$$

Therefore, $\mathcal{T}$ is a contraction operator on X. This also implies the continuity of $\mathcal{T}$.

From the above results, we deduce the following theorem.

Theorem 1. The mixed integral equation (1.1) has a unique solution in X under assumptions (1)–(4) of Section 3, provided that (4.3) holds.

Proof. The proof follows directly from Lemmas 4.1 and 4.2. Indeed, under the condition

$$BM_G < \mu,$$

the operator $\mathcal{T}\Phi = (f + L\Phi)/\mu$ maps the ball $B_r \subset X$ into itself and is a contraction. Moreover, Lemma 4.1 guarantees that it is a well-defined self-map of the complete Banach space X, and Lemma 4.2 shows that it is contractive on all of X. Therefore, by Banach's fixed-point theorem, $\mathcal{T}$ has a unique fixed point $\Phi \in X$. This fixed point satisfies $\mu\Phi = f + L\Phi$, and hence it is the unique solution of (1.1).

5. The convergence of the solution

It is very important to study the convergence of the solution, especially when semi-analytical or numerical methods are used for obtaining approximate solutions. The convergence analysis guarantees that the approximate solution converges to the exact solution as the number of terms, iterations, or discretization points increases. Therefore, the numerical results without convergence are not reliable and may not have the physical significance required in applied models.

Furthermore, the convergence analysis provides information on the stability, accuracy, and efficiency of the proposed method. It can be used to predict the approximation error and to guarantee that the computed solution accurately describes the behavior of the mathematical model. This is of particular importance in applied and physical sciences. For this purpose, consider the successive approximation sequence $\{\Phi_1(x,t), \Phi_2(x,t), \ldots, \Phi_n(x,t), \ldots\}$. Using Eq (1.1), we obtain

$$\mu(\Phi_n - \Phi_{n-1})(x,t) = \int_0^t \int_{-1}^1 G(t,\tau)K(x,y)(\Phi_{n-1} - \Phi_{n-2})(y,\tau)\,dy\,d\tau. \tag{5.1}$$

Consider

$$\Phi_n(x,t) = \sum_{i=0}^{n} \Psi_i(x,t), \tag{5.2}$$

where

$$\Psi_n(x,t) = \Phi_n(x,t) - \Phi_{n-1}(x,t), \qquad \Psi_0(x,t) = \frac{f(x,t)}{\mu}, \qquad n \geq 1. \tag{5.3}$$

Thus, Eq (5.1) takes the form

$$\mu\Psi_n(x,t) = \int_0^t \int_{-1}^1 G(t,\tau)K(x,y)\Psi_{n-1}(y,\tau)\,dy\,d\tau. \tag{5.4}$$

Now, we consider the following lemma.

Lemma 5.1. The sequence $\{\Phi_n\}$ defined by (5.2) converges in the X-norm provided that

$$BM_G < \mu.$$

Proof. From Eq (5.4) and the estimate established in Lemma 4.1, we obtain

$$\|\Psi_n\|_X \leq \frac{BM_G}{\mu}\|\Psi_{n-1}\|_X. \tag{5.5}$$

Setting

$$\rho = \frac{BM_G}{\mu} < 1,$$

and applying the estimate recursively, we obtain

$$\|\Psi_n\|_X \leq \rho^n\|\Psi_0\|_X = \rho^n\frac{\|f\|_X}{\mu}. \tag{5.6}$$

Hence,

$$\sum_{n=0}^{\infty}\|\Psi_n\|_X < \infty,$$

and therefore the series

$$\sum_{n=0}^{\infty}\Psi_n$$

converges in the Banach space X. Consequently, Φ_n converges in the X-norm to the unique solution Φ.

Moreover, the truncation error satisfies

$$\|\Phi - \Phi_n\|_X \leq \frac{\|f\|_X}{\mu}\frac{\rho^{n+1}}{1-\rho}. \tag{5.7}$$

Thus, the successive approximation converges geometrically in the X-norm.

6. The error study

Error analysis is crucial for the analysis of integral equations, since it provides a quantitative measure of the difference between the exact and approximate solutions. Error analysis helps us to determine the accuracy, stability, and reliability of the numerical method proposed. In addition, it ensures that the computed solution approximates the exact solution. There are several types of errors that researchers need to be aware of.

(1) Errors occurring in the approximation process, including truncation errors due to finite approximation series, errors due to numerical integration or discretization procedures, approximation errors due to finite-precision calculations, and approximation errors associated with polynomial or spectral representations.
(2) Method-related errors.
(3) Errors resulting from the software used.

Scientifically, the error function is defined as the difference between the exact solution and the approximate solution. It is noteworthy that this error equation is itself an integral equation with a structure similar to that of the original problem. Therefore, existence and uniqueness theorems can be applied to it, and convergence studies can be conducted. It is also noteworthy that the error equation has a unique solution.

Consider that the equation of the numerical solution takes the form

$$\mu\Phi_m(x,t) = f_m(x,t) + \int_0^t \int_{-1}^1 G(t,\tau)K(x,y)\Phi_m(y,\tau)\,dy\,d\tau. \tag{6.1}$$

The error function takes the form $R_m(x,t) = \Phi(x,t) - \Phi_m(x,t)$, and the error integral equation becomes

$$\mu R_m(x,t) = [f(x,t) - f_m(x,t)] + \int_0^t \int_{-1}^1 G(t,\tau)K(x,y)R_m(y,\tau)\,dy\,d\tau. \tag{6.2}$$

It is noteworthy that the integral error equation (6.2), under the same conditions as the original integral equation (1.1), has a unique solution under the same condition defined by inequality (4.3). The convergence of this error can also be proven. The convergence statement concerns perturbations of the source term while the continuous integral operator remains fixed. In particular, convergence of the error requires $\|f - f_m\|_X \to 0$. Merely increasing the number of spatial subdivisions does not establish this condition or prove convergence of the Nyström discretization in Section 8.

The error equation (6.2) satisfies the same operator estimate as the original problem. Hence, using the estimate established in Lemma 4.1, we obtain

$$\|R_m\|_X \le \frac{\|f - f_m\|_X}{\mu - BM_G}, \qquad BM_G < \mu. \tag{6.3}$$

Consequently, if

$$\|f - f_m\|_X \longrightarrow 0 \qquad \text{as } m \to \infty,$$

then

$$\|R_m\|_X = \|\Phi - \Phi_m\|_X \longrightarrow 0.$$

Thus, convergence of the approximation follows whenever the approximation of the free term is consistent in the X-norm.

Also, we can write the error integral equation (6.2) in the integral operator form

$$(\mu I - W)R_m = H, \qquad H = H(x,t) = f(x,t) - f_m(x,t), \tag{6.4}$$

where

$$(WR_m)(x,t) = \int_0^t \int_{-1}^1 G(t,\tau)K(x,y)R_m(y,\tau)\,dy\,d\tau. \tag{6.5}$$

Moreover, we can easily prove the following lemmas.

Lemma 6.1. The integral operator W, defined by Eq (6.5), maps the space $X = C([0,T]; L^2(-1,1))$ into itself. The radius of the ball B_r takes the form $r = \frac{\|H\|_X}{\mu - BM_G}$.

The proof follows from the same operator estimate used in Lemma 4.1.

Lemma 6.2. The integral operator W, defined by Eq (6.5), is continuous in the Banach space $X = C([0,T]; L^2(-1,1))$. Moreover, the associated fixed-point operator is a contraction under the condition $BM_G < \mu$.

The proof follows directly from the contraction argument of Lemma 4.2.

Lemma 6.3. For the iteration $\{R_{m_1}(x,t), R_{m_2}(x,t), \ldots, R_{m_n}(x,t), \ldots\} \subset R_m(x,t)$, the sequence $\{R_m(x,t)\}$ of Eq (6.5) is uniformly convergent under the condition $BM_G < \mu$.

The proof is analogous to that of Lemma 5.1 and follows from the successive-approximation argument.

Lemma 6.4. As $m \to \infty$, the error $R_m(x,t) \to 0$.

Proof. If

$$\|H_m\|_X \longrightarrow 0 \qquad \text{as } m \to \infty,$$

then, using the stability estimate,

$$\|R_m\|_X \leq \frac{\|H_m\|_X}{\mu - BM_G},$$

and consequently

$$\|R_m\|_X \longrightarrow 0.$$

7. Method for separating variables and the physical interpretation of the second-kind integral equation with a time relationship

The unknown function in problems of mathematical physics depends on space and time. Researchers are mainly interested in determining this unknown function. Thus, there are several methods for finding this unknown function, such as the time partition method. This method transforms the integral equation in position and time into a system of integral equations in position. Another common method of solution assumes that the time function is multiplied by the position function. This assumption is very important in mixed fractional integral equations. The third method consists of transforming non-homogeneous integral equations with time-dependent coefficients into a class of integral equations with only time-dependent coefficients. This method decouples the integral equation from the time component, which makes it easier to solve. Moreover, it allows researchers to improve the choice of the time function.

Assume

$$\Phi(x,t) = N(t)\phi(x), \qquad f(x,t) = f_1(x)M(t). \tag{7.1}$$

Using Eq (7.1) in Eq (1.1), we obtain

$$\mu\phi(x) - \lambda(t)\int_{-1}^{1} K(x,y)\phi(y)\,dy = V(x,t), \tag{7.2}$$

where

$$\lambda(t) = \frac{1}{N(t)}\int_0^t G(t,\tau)N(\tau)\,d\tau, \qquad V(x,t) = \frac{M(t)}{N(t)}f_1(x).$$

For the numerical choice

$$G(t,\tau) = \frac{1}{4}t^2\tau^2, \qquad N(t) = t,$$

the time-dependent coefficient becomes

$$\lambda(t) = \frac{1}{N(t)} \int_0^t G(t,\tau)N(\tau)\,d\tau = \frac{t^5}{16}.$$

It is observed that when the assumed time function for the unknown function is the same as that of the free function, the integral equation takes the following form:

$$\mu\phi(x) - \lambda(t) \int_{-1}^{1} K(x,y)\phi(y)\,dy = f_1(x). \tag{7.3}$$

In Eqs (7.2) and (7.3), provided that the spatial kernel has a finite Hilbert–Schmidt norm and $\lambda(t) \neq 0$, a sufficient contraction condition for the fixed-time spatial Fredholm equation is

$$\left\{ \int_{-1}^{1} \int_{-1}^{1} K^2(x,y)\,dx\,dy \right\}^{1/2} < \left| \frac{\mu}{\lambda(t)} \right|. \tag{7.4}$$

Writing $B = (\int_{-1}^{1} \int_{-1}^{1} K^2(x,y)\,dx\,dy)^{1/2}$, we have $\|\mathcal{S}\|_{L^2\to L^2} \leq B$. Thus, for $\mu > 0$, inequality (7.4) is equivalent to $|\lambda(t)|B < \mu$, which makes the fixed-time spatial mapping contractive. This is distinct from the contraction condition $BM_G < \mu$ for the original mixed Volterra–Fredholm operator.

For the numerical choice specified above, $M_G = \sup_{0\leq t\leq T} \int_0^t |G(t,\tau)|\,d\tau = T^5/12$ and $\lambda(t) = t^5/16$. Consequently, for $0 < t \leq T$, $|\lambda(t)| \leq \frac{3}{4}M_G$, so the mixed-equation condition $BM_G < \mu$ implies the fixed-time spatial condition when $B < \infty$. This implication is sufficient, not a general equivalence, and does not establish the Hilbert–Schmidt assumption for every singular kernel. At $t = 0$, the continuous extension $\lambda(0) = 0$ reduces the spatial equation to $\mu\phi = f_1$.

7.1. Physical interpretations of the integral equation

The integral equation (7.3), together with its integral structure, may be interpreted as a mathematical representation of nonlocal interactions with a prescribed time-dependent coupling, rather than as a model derived directly from governing physical equations. The method used to separate the variables provides a parameter-dependent spatial formulation. Therefore, the physical structure can be interpreted illustratively as follows:

The given free function may represent a prescribed external influence, such as an electric field, a magnetic field, or a thermal gradient, depending on the physical application.

The integral kernel mathematically characterizes the nonlocal spatial interaction between different points of the domain. Its interpretation as a physical interaction potential would require additional modeling assumptions.

The integral influence represents the combined nonlocal contributions of different spatial points, describing mathematically how the solution at one location is coupled to its values at other locations.

The time coupling coefficient controls the relative contribution of the spatial integral operator as time varies. Its variation reflects the response of the prescribed mathematical model and does not, by itself, establish physical energy accumulation, equilibrium, or stabilization.

These interpretations are intended only as illustrative physical analogies. A derivation from governing physical equations, identification of physical parameters, and validation against experimental data are beyond the scope of the present study.

8. Discussion of the solution to the Fredholm integral equation for kernels derived from the hypergeometric kernel and its relationship to time

Consider the integral equation

$$\mu\phi(x) - \lambda(t)\int_{-1}^{1} K(x,y)\phi(y)\,dy = f_1(x), \qquad -1 \le x \le 1. \tag{8.1}$$

The Hilbert–Schmidt-based results of Sections 3–4 apply to the Carleman examples and the two selected general hypergeometric cases, for which the required square-integrability condition holds. The complete elliptic example and the unregularized logarithmic kernel do not satisfy that condition on the full interval; the corresponding fixed-time numerical experiments are not presented as direct applications of the full-domain Hilbert–Schmidt theorem.

For the product-integration form used in the condition-number assessment, partition the spatial domain into cells $I_j = [a_j, a_{j+1}]$, $j = 0, \dots, N-1$, where

$$-1 = a_0 < a_1 < \cdots < a_N = 1, \qquad x_j = \frac{a_j + a_{j+1}}{2}.$$

The logarithmic example uses the corresponding partition of the regularized domain described below.

Approximating the density on each cell by its midpoint value gives the product-integration collocation system

$$\mu\phi(x_k) - \lambda(t)\sum_{j=0}^{N-1} Q_{kj}\phi(x_j) = f_1(x_k), \qquad k = 0, 1, \dots, N-1, \tag{8.2}$$

with the singularity-aware matrix entries

$$Q_{kj} = \int_{I_j} K(x_k, \xi)\,d\xi.$$

The kernel is integrated over each cell, including any integrable singularity at $\xi = \pm x_k$, rather than sampled at $\xi = x_k$. For an even density and a kernel even in its second argument, reduction to the positive half interval yields the matrix used in Section 8.3, with

$$Q^{+}_{ij} = 2\int_{j/n}^{(j+1)/n} K(x_i, \xi)\,d\xi, \qquad x_i = \frac{i + \frac{1}{2}}{n}, \quad i, j = 0, \dots, n-1.$$

Here, the full-interval partition has $N = 2n$ cells when the two halves use equal meshes.

For reproducibility, the cell integrals in the product-integration matrix are evaluated by Gauss–Legendre quadrature after isolating any cell containing or touching a singular point. For an even solution and kernel, the integration over the symmetric domain is reduced to the positive half, so that

$$Q_{ij} = 2\int_{a_j}^{b_j} K(x_i, \xi)\,d\xi, \qquad x_i = \frac{a_i + b_i}{2}.$$

A cell with $x_i \in [a_j, b_j]$ is split at $\xi = x_i$. On each nonempty side, we apply the change of variable

$$\xi = x_i \pm Ls^{\alpha}, \qquad 0 < s < 1, \qquad |d\xi| = \alpha L s^{\alpha-1}\,ds,$$

where L is the distance from x_i to the relevant cell endpoint. We use $\alpha = 2$ for the logarithmic kernel, $\alpha = 5$ for the Carleman kernel $K(x_i, \xi) = |x_i^2 - \xi^2|^{-p}$, and $\alpha = 6$ for the general hypergeometric kernel. Thus, no pointwise sampling at the singularity is required. For the logarithmic and Carleman kernels, the singular factors are evaluated using the positive transformed distance directly, not by subtracting nearly equal floating-point coordinates. The logarithmic example uses $D_\delta = [-1, -\delta] \cup [\delta, 1]$, $\delta = 0.1$.

For the complete elliptic kernel, the equivalent positive-half representation

$$K(x, \xi) = \frac{2}{\pi \max(x, \xi)} K_{\text{ell}}\left(\frac{\min(x, \xi)}{\max(x, \xi)}\right)$$

is integrated separately on either side of $\xi = x$. The ratio variable $u = \min(x, \xi)/\max(x, \xi)$ is used; for a transformed interval ending at $u = 1$, the substitution $u = 1 - (1 - u_0)s^2$ resolves the logarithmic endpoint singularity of the complete elliptic integral. In MATLAB, ellipke(u^2) is evaluated with the parameter $m = u^2$. For the general hypergeometric case, the Gauss function is evaluated by its power series for $z \leq 1/2$ and by its standard continuation in $1 - z$ for $z > 1/2$, avoiding a slowly convergent series near $z = 1$.

The Gauss–Legendre orders for ordinary/singularity-adjacent cells are respectively $(80, 64)$ for logarithmic, $(64, 56)$ for Carleman, $(64, 64)$ for complete elliptic, and $(48, 56)$ for general hypergeometric kernels. The solutions are computed at $t = 0.01, 0.4, 0.9$ with $\lambda(t) = t^5/16$. The logarithmic plots compare $n = 160$ and $n_{\text{ref}} = 320$ positive-half cells, whereas the remaining plotted cases use $n = 80$ and $n_{\text{ref}} = 160$. In the error plots, the refined solution is evaluated at the coarse-grid nodes by the same continuous product-integration extension.

Case 1: The logarithmic kernel and analysis of its results

When $p = 1$ and $q = 3$, the hypergeometric kernel reduces to the logarithmic kernel already obtained in Equation (2.1), namely

$$K(x_i, x_j) = \frac{1}{2x_i x_j} \ln\left|\frac{x_i + x_j}{x_i - x_j}\right|. \tag{8.3}$$

For the logarithmic kernel, the product-integration form of the discrete system is

$$\mu\phi(x_k) - \lambda(t) \sum_{j=0}^{N-1} Q_{kj}^{\log} \phi(x_j) = f_1(x_k), \tag{8.4}$$

where the domain is partitioned into cells contained in D_δ, and

$$Q_{kj}^{\log} = \int_{I_j} \frac{1}{2x_k \xi} \ln\left|\frac{x_k + \xi}{x_k - \xi}\right| d\xi.$$

All retained collocation points satisfy $|x_k| \geq \delta$.

8.1. Studying the effect of time on the logarithmic kernel

From the numerical results of Eq (8.4), we deduce that converting the hypergeometric kernel to its logarithmic form leads to a significant simplification of the numerical calculation process while preserving the fundamental properties of the kernel. It is a symmetric kernel with a logarithmic

singularity on the diagonal $x_i = x_j$. For the numerical computations, the regularized symmetric domain $D_\delta = [-1, -\delta] \cup [\delta, 1]$, with $\delta = 0.1$, is used to avoid the strong singular behavior near the origin. Owing to symmetry, only the positive branch is displayed in the figures. The results also show that the numerical solution depends directly on the value of time t, as this parameter determines the contribution of the integral term compared with the free term x^2. When $t = 0.01$, the time-dependent coefficient is $\lambda(t) = 6.25 \times 10^{-12}$. Here, the effect of the integral operator is negligible and the solution curve is almost identical to the free function x^2. For $t = 0.4$, we have $\lambda(t) = 6.4 \times 10^{-4}$, so the effect of the integral term remains weak compared with the free term. Hence, the solution remains very close to x^2. For $t = 0.9$, we have $\lambda(t) = 3.6905625 \times 10^{-2}$. The contribution of the integral term becomes more noticeable, and the solution deviates further from the reference curve x^2, as shown in Figure 1. Here, the effect of the logarithmic singularity is more prominent, especially when the values of x and ξ are close to each other. The logarithm changes rapidly when the denominator approaches zero. This requires a denser numerical mesh to accurately describe this behavior. The estimated mesh-refinement difference compares the spatial solutions obtained with $n = 160$ and $n_{\text{ref}} = 320$ positive-half cells, respectively, with the refined solution evaluated at the coarse-grid nodes, as shown in Figure 2.

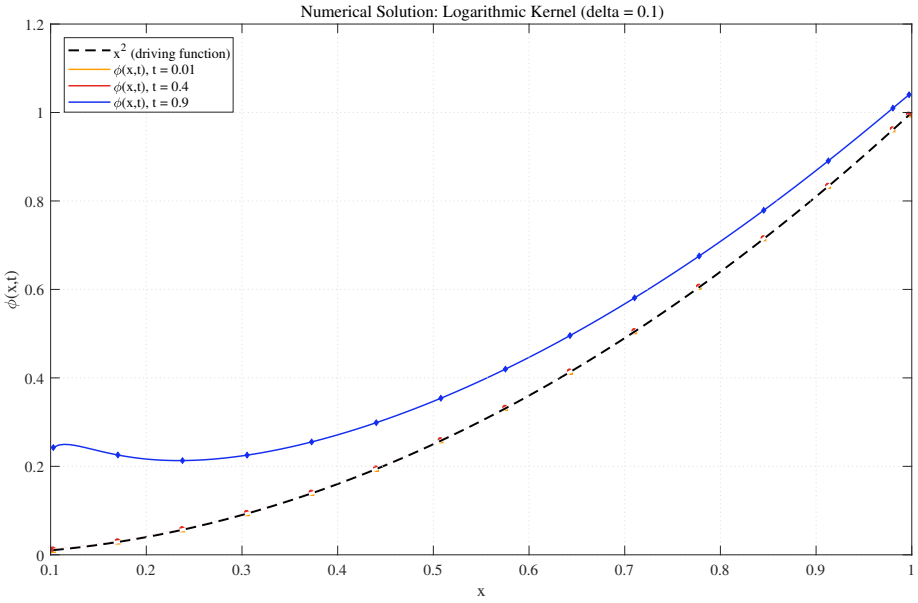


Figure 1. The numerical spatial solution $\phi(x, t)$ for the logarithmic kernel on $0.1 \leq x \leq 1$, using $n = 160$ positive-half cells, at $t = 0.01, 0.4, 0.9$. The dashed curve denotes x^2.

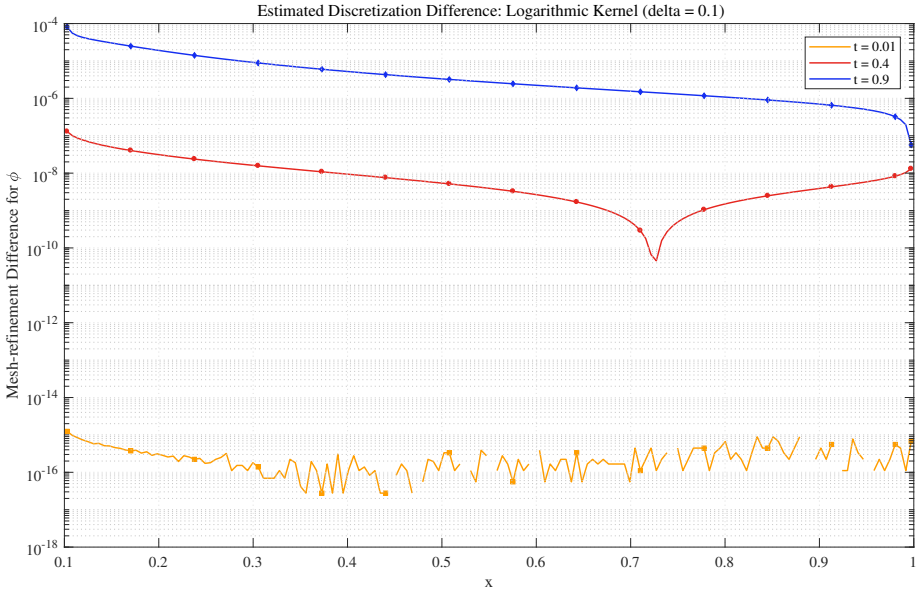


Figure 2. The estimated mesh-refinement difference $E_{160,320}(x_i, t) = |\phi_{160}(x_i, t) - \phi^{\text{ext}}_{320}(x_i, t)|$ for the logarithmic kernel at $t = 0.01, 0.4, 0.9$. The refined solution is evaluated at coarse nodes; the vertical scale is logarithmic.

Scientific conclusion: From the preceding results, we conclude that the logarithmic kernel retains its integral property despite its singular behavior. However, it should be noted that this singularity imposes numerical requirements that increase as the strength of the time-dependent coefficient increases. Therefore, the accuracy of the solution is also determined by the ability of the numerical mesh to represent the sharp logarithmic behavior near the diagonal $x = \xi$.

Case (2): Weakly singular Carleman kernel and analysis of its results

To obtain the Carleman kernel from the hypergeometric function, we assume in Eq (1.1) that $0 < p < 1$ and $q = p + 1$. Hence, the kernel takes the form

$$K(\xi, x) = \frac{1}{(\xi^2 + x^2)^p} F\left(\frac{p}{2}, \frac{p+1}{2}, \frac{p+1}{2}; \frac{4\xi^2 x^2}{(\xi^2 + x^2)^2}\right). \tag{8.5}$$

For the Carleman kernel, the corresponding product-integration linear system associated with (8.2) takes the form

$$\mu\phi(x_k) - \lambda(t) \sum_{j=0}^{N-1} Q^{\text{C}}_{kj} \phi(x_j) = f_1(x_k), \tag{8.6}$$

where

$$Q^{\text{C}}_{kj} = \int_{I_j} |x_k^2 - \xi^2|^{-p} \, d\xi, \qquad 0 < p < 1.$$

The integrable singularities at $\xi = \pm x_k$ are treated inside the cell integrals.

Figure 3 displays the Carleman numerical solution for $p = 0.01$.

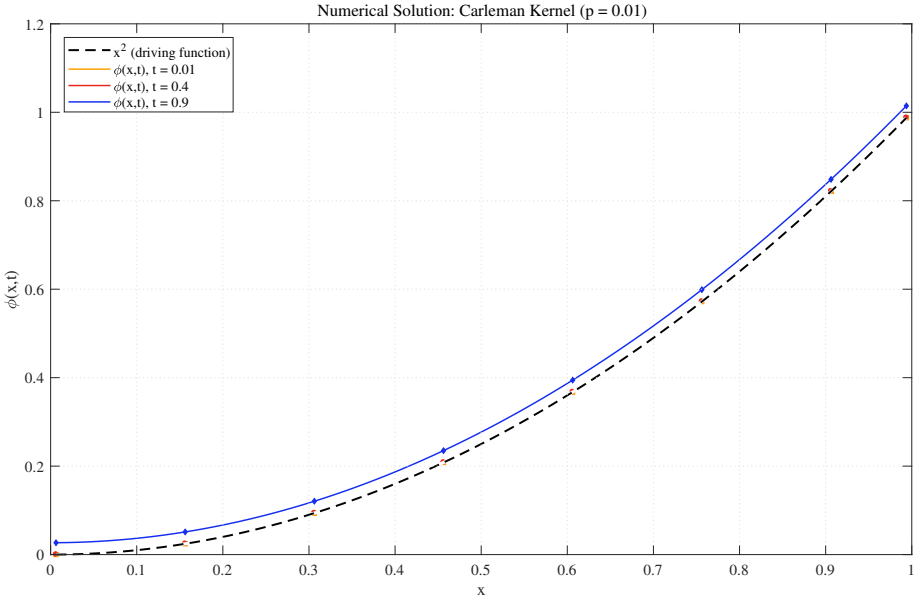


Figure 3. The spatial numerical solution $\phi(x,t)$ for the Carleman kernel with $p = 0.01$ and $n = 80$, at $t = 0.01, 0.4, 0.9$. The dashed curve denotes x^2.

Figure 4 reports the corresponding mesh-refinement differences for $p = 0.01$.

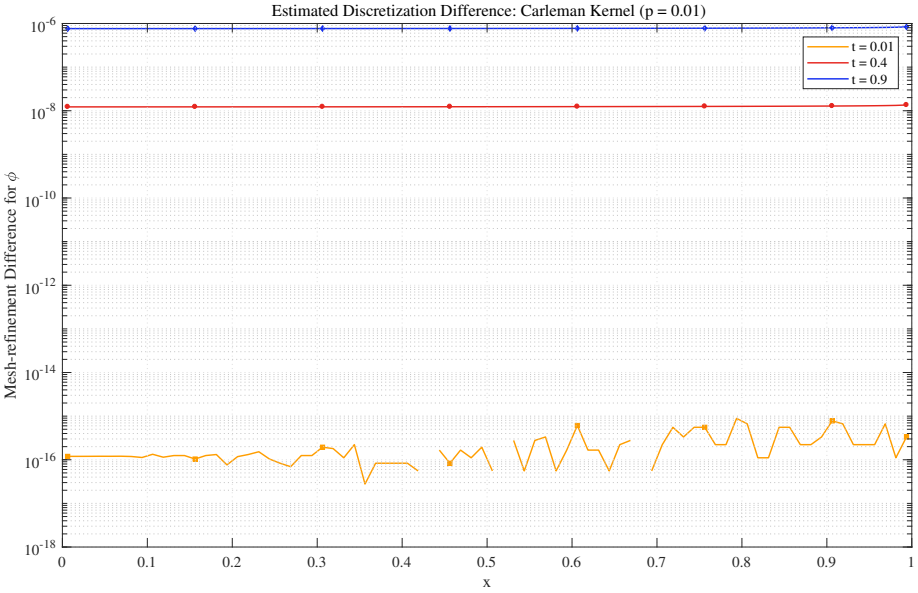


Figure 4. The estimated mesh-refinement difference $E_{80,160}(x_i,t) = |\phi_{80}(x_i,t) - \phi^{\text{ext}}_{160}(x_i,t)|$ for the Carleman kernel with $p = 0.01$ at $t = 0.01, 0.4, 0.9$. The vertical scale is logarithmic.

Figure 5 displays the Carleman numerical solution for $p = 0.4$.

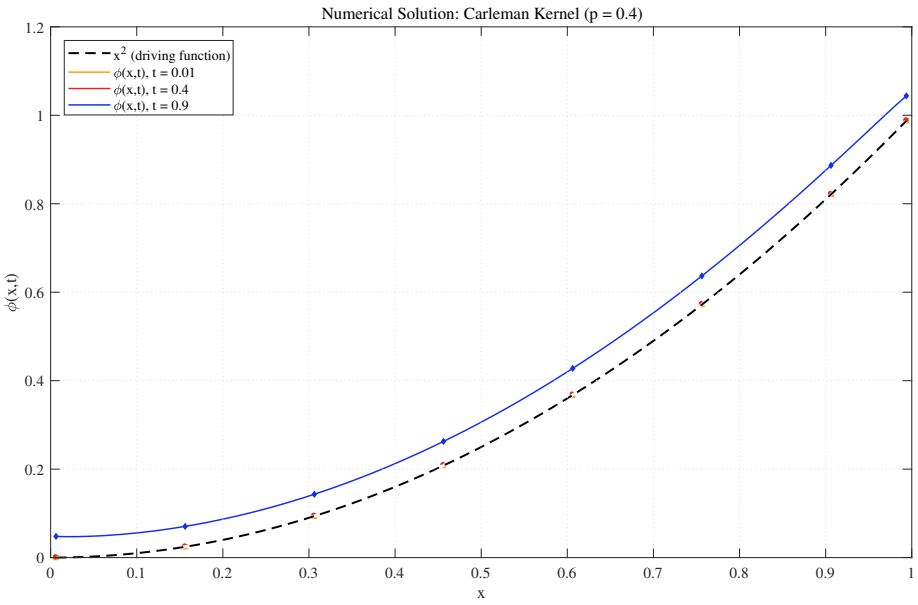


Figure 5. The numerical spatial solution $\phi(x,t)$ for the Carleman kernel with $p = 0.4$ and $n = 80$, at $t = 0.01, 0.4, 0.9$. The dashed curve denotes x^2.

Figure 6 reports the corresponding mesh-refinement differences for $p = 0.4$.

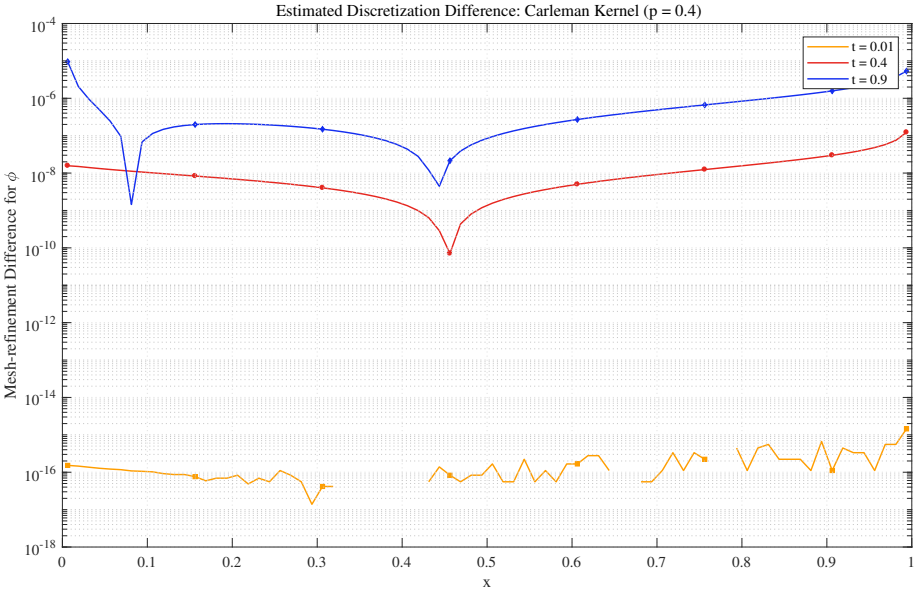


Figure 6. The estimated mesh-refinement difference $E_{80,160}(x_i,t) = |\phi_{80}(x_i,t) - \phi^{\text{ext}}_{160}(x_i,t)|$ for the Carleman kernel with $p = 0.4$ at $t = 0.01, 0.4, 0.9$. The vertical scale is logarithmic.

The estimated mesh-refinement differences remain small for the three selected times and generally increase as the time-dependent coefficient becomes larger. Differences at $t = 0.01$ are near floating-point roundoff and should not be used independently to infer a convergence rate.

8.2. The physical interpretation of time for the Carleman kernel

After using Eq (8.6) when $\mu = 1$ and $f_1(x_k) = x_k^2$, at different times $t = 0.01$, 0.4, and 0.9, we give the following discussion:

(1) At the early time phase $t = 0.01$, the time-dependent coefficient is $\lambda(t) = 6.25 \times 10^{-12}$, which makes the contribution of the integral term very small. For the two tested values of p, the spatial solution remains close to x^2.
(2) When we choose the intermediate time $t = 0.4$, we observe that the time value $\lambda(t)$ begins to grow, and the computed solution shows a slightly larger deviation from the prescribed free function. This numerical change does not, by itself, establish energy accumulation.
Given the importance of this intermediate time, it can be said that, for a weak singularity $p = 0.01$, the local interaction is weak and the kernel is nearly flat. In this test, the weaker singularity corresponds to a relatively small numerical deviation from the prescribed free function; no physical dispersion or accumulation mechanism is inferred. At $p = 0.4$, the kernel becomes more pronounced near the points $x_k = x_j$, and the numerical solution shows a more noticeable deviation from the free function as the time-dependent coefficient increases. A mesh-refinement check is therefore appropriate for this stronger singularity.
(3) However, at $t = 0.9$, we observe that the time value $\lambda(t)$ has increased, and its impact on the integral part has also increased. The numerical solution therefore shows a more noticeable deviation from the free function as the contribution of the integral term increases.

For the two parameter values tested, the numerical response may be summarized as follows:

a- At $p = 0.01$, the kernel is weakly singular, and the numerical solution remains relatively close to the free function.
b- At $p = 0.4$, the stronger singularity is associated with a more noticeable influence of the integral term on the numerical solution.

Case (3): Weakly singular elliptic kernel and analysis of its results

In the case of the elliptic kernel, we assume in the hypergeometric kernel that $p = \frac{1}{2}$ and $q = 2$.

Analysis and interpretation of the time effect: We note that we chose three values for time, namely $t = 0.01$, 0.4, and 0.9. These times are selected to provide a simplified view of the potential function $\Phi(x, t) = \phi(x)N(t)$, how it is employed, and its connection to the free function $f(x, t) = f(x)N(t)$.

At very short intervals ($t = 0.01$), it is observed that the extremely small value of the time parameter $\lambda(t)$ makes the effect of the integral operator almost negligible. Consequently, the scaled numerical solution $\Phi(x, t) = t\phi(x, t)$ is close to the scaled free term tx^2, for $\mu = 1$.

At time ($t = 0.4$), we find that the growth of the time parameter increases the influence of the integral operator. The scaled numerical solution shows only a slight deviation from tx^2.

At time ($t = 0.9$), the larger value of the time-dependent coefficient increases the influence of the integral operator. The numerical solution remains smooth and shows a more noticeable deviation from the scaled free term tx^2, particularly as x approaches one. Representative numerical values for the complete elliptic kernel are reported in Table 1.

Table 1. Representative numerical values of $\Phi(x,t) = \phi(x)N(t)$ for the complete elliptic kernel.

x	$\Phi(x, 0.01)$	$\Phi(x, 0.4)$	$\Phi(x, 0.9)$
0.00625	3.9063×10^{-7}	0.0002739	0.0570744
0.20625	4.2539×10^{-4}	0.0172833	0.0826476
0.40625	0.0016504	0.0662986	0.1925192
0.60625	0.0036754	0.1473084	0.3746061
0.80625	0.0065004	0.2603016	0.6268528
0.99375	0.0098754	0.3952522	0.9231708

The numerical scaled solution for the complete elliptic kernel is presented in Figure 7.

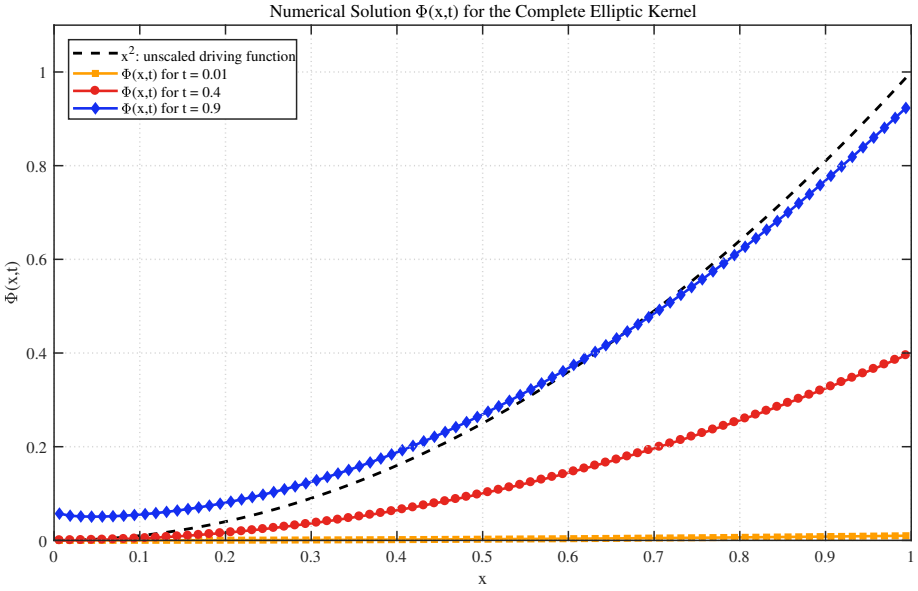


Figure 7. The numerical scaled solution $\Phi(x,t) = t\phi(x,t)$ for the complete elliptic kernel with $p = 1/2$, $q = 2$, $\mu = 1$, $n = 80$, at $t = 0.01, 0.4, 0.9$. The dashed curve represents the unscaled reference x^2, not the source tx^2.

The corresponding mesh-refinement differences for the complete elliptic kernel are presented in Figure 8.

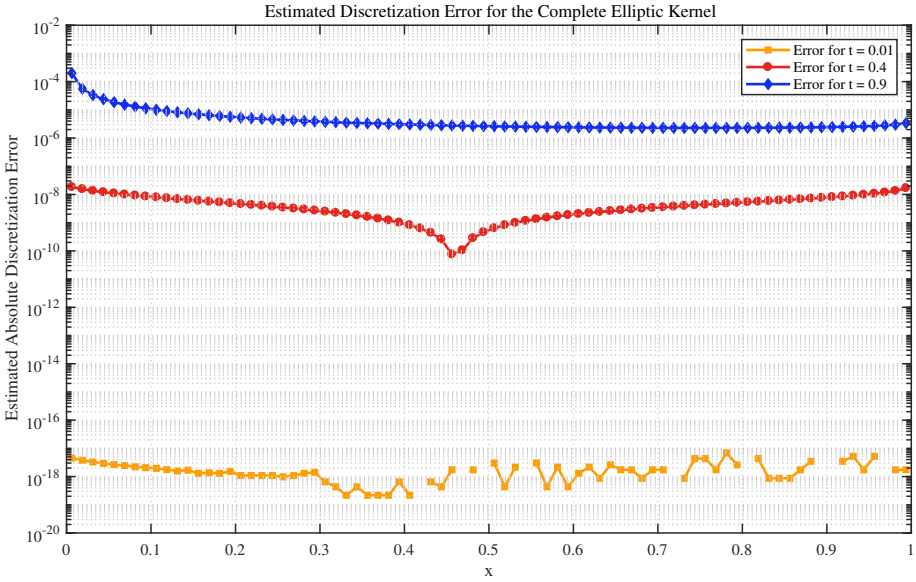


Figure 8. The estimated mesh-refinement difference $E_{80,160}(x_i, t) = |\Phi_{80}(x_i, t) - \Phi^{\text{ext}}_{160}(x_i, t)|$ for the complete elliptic kernel with $p = 1/2$, $q = 2$, $\mu = 1$, at $t = 0.01, 0.4, 0.9$. The vertical scale is logarithmic; early-time differences are near floating-point roundoff.

8.3. Numerical validation and comparison with a Galerkin method

To provide an independent validation of the adopted numerical discretization, the weighted quadrature-based Nyström-type method is compared with a standard piecewise-constant Galerkin method [14]. The comparison is performed for the retained Carleman cases $p = 0.01$ and $p = 0.4$, and for the complete elliptic kernel.

The comparison is carried out at $T = 0.9$, for which

$$\lambda(T) = \frac{T^5}{16}.$$

A manufactured exact solution is prescribed as

$$\psi(x) = (1 - x^2)\,(2 + \cos(4\pi x))\,, \tag{8.7}$$

and the corresponding source term is constructed independently as

$$f_*(x) = \mu\psi(x) - \lambda(T)(\mathcal{S}\psi)(x), \tag{8.8}$$

where $\mathcal{S}$ denotes the corresponding spatial integral operator.

For the independent numerical verification, the continuous integral $(\mathcal{S}\psi)(x) = \int_{-1}^{1} K(x, \xi)\psi(\xi)\, d\xi$ is evaluated by refined, singularity-aware quadrature. The Galerkin load entries are then assembled by integrating this continuous source against the piecewise-constant test functions, independently of the Galerkin system matrix. Thus, the manufactured source is not obtained by applying a discrete Galerkin matrix to the sampled exact solution.

Both numerical methods are applied using the same number n of independent spatial coefficients. The error is measured by

$$E_2 = \|\phi_n - \psi\|_{L^2(-1,1)}.$$

The apparent equality of the three Galerkin error columns at the reported precision is mainly explained by the common piecewise-constant approximation error. Let P_n denote the $L^2(-1,1)$-orthogonal projection onto the corresponding piecewise-constant space. By orthogonality,

$$\|\psi - \phi_n^{\mathrm{G}}\|_{L^2}^2 = \|\psi - P_n\psi\|_{L^2}^2 + \|P_n\psi - \phi_n^{\mathrm{G}}\|_{L^2}^2.$$

The kernel-independent projection term dominates these errors. For example, at $n = 10$, the independently assembled Galerkin systems give errors of approximately 0.275775, 0.275805 and 0.275936 for Carleman $p = 0.01$, Carleman $p = 0.4$ and the complete elliptic kernel, respectively. All three round to 2.76×10^{-1}. Hence the equal entries in the table reflect the displayed precision, not identical Galerkin solutions.

The results in Table 2 show decreasing errors over the tested spatial refinement levels for both numerical discretizations. For the present smooth manufactured solution, the Nyström-type method exhibits substantially smaller L^2-errors than the piecewise-constant Galerkin approximation. The error reduction of the Nyström approximation is particularly clear for the weak Carleman case and the complete elliptic kernel, while the stronger Carleman singularity at $p = 0.4$ leads to a somewhat slower error reduction.

Table 2. Manufactured-solution $L^2(-1,1)$ errors at $T = 0.9$. C denotes the Carleman kernel, and n denotes the number of independent positive-half spatial coefficients.

	Nyström-type method			Piecewise-constant Galerkin		
n	C, $p = 0.01$	C, $p = 0.4$	Elliptic	C, $p = 0.01$	C, $p = 0.4$	Elliptic
10	2.96×10^{-4}	5.27×10^{-3}	8.68×10^{-3}	2.76×10^{-1}	2.76×10^{-1}	2.76×10^{-1}
20	7.14×10^{-5}	1.46×10^{-3}	1.89×10^{-3}	1.41×10^{-1}	1.41×10^{-1}	1.41×10^{-1}
40	1.77×10^{-5}	4.43×10^{-4}	4.28×10^{-4}	7.06×10^{-2}	7.06×10^{-2}	7.06×10^{-2}
80	4.41×10^{-6}	1.40×10^{-4}	1.00×10^{-4}	3.53×10^{-2}	3.53×10^{-2}	3.53×10^{-2}

The geometric convergence and source-perturbation estimates in Sections 5–6 concern the continuous integral operator and do not, by themselves, establish convergence of the spatial Nyström scheme. For the fixed-time manufactured-source problem, define the continuous residual of the extended numerical approximation by

$$r_n(x) = f_*(x) - \mu\phi_n(x) + \lambda(T)(\mathcal{S}\phi_n)(x).$$

Whenever the continuous spatial operator $\mathcal{S} : L^2(-1,1) \to L^2(-1,1)$ is bounded and $|\lambda(T)|\|\mathcal{S}\|_{2\to 2} < \mu$, the manufactured exact solution satisfies the conditional estimate

$$\|\psi - \phi_n\|_{L^2(-1,1)} \le \frac{\|r_n\|_{L^2(-1,1)}}{\mu - |\lambda(T)|\|\mathcal{S}\|_{2\to 2}}.$$

Thus, a general spatial-convergence statement additionally requires an independently justified consistency condition $\|r_n\|_{L^2(-1,1)} \to 0$ and verification of the operator bound for the particular kernel.

Neither requirement follows from the contraction argument alone. The decreasing errors in Table 2 provide numerical evidence for the tested manufactured solution, not a general Nyström convergence theorem.

The following conditioning assessment concerns the fixed-time Fredholm system in Eq (8.1). For the condition-number assessment, we use an even-symmetric midpoint product-integration discretization of the spatial integral operator. On the positive half interval, let $I_j = [j/n, (j+1)/n]$ and $x_i = (i + \frac{1}{2})/n$, $i, j = 0, \ldots, n-1$. The collocation matrix is defined by

$$A_n^{\mathrm{N}} = \mu I_n - \lambda(T) Q_n, \qquad (Q_n)_{ij} = 2 \int_{I_j} K(x_i, \xi)\, d\xi. \tag{8.9}$$

To evaluate the continuous error norm, the Nyström approximation is extended away from the collocation nodes by the same integral representation:

$$\phi_n(x) = \frac{1}{\mu}\left[f_*(x) + \lambda(T) \sum_{j=0}^{n-1} Q_j(x) \phi_n(x_j) \right], \qquad Q_j(x) = 2 \int_{I_j} K(x, \xi)\, d\xi.$$

The reported error is then evaluated over the full symmetric interval, with a refined quadrature for the continuous error integral.

For the piecewise-constant Galerkin comparator with the same positive-half cells and their even extensions, the matrix is

$$\begin{aligned} A_n^{\mathrm{G}} &= \mu M_n - \lambda(T) S_n, \\ (M_n)_{ij} &= \frac{2}{n} \delta_{ij}, \\ (S_n)_{ij} &= 4 \int_{I_i} \int_{I_j} K(x, \xi)\, d\xi\, dx. \end{aligned} \tag{8.10}$$

Integrals over cells containing a singularity are evaluated using singularity-aware integration rather than pointwise diagonal sampling. Condition numbers are computed in the spectral matrix norm, namely

$$\mathrm{cond}_2(A) = \|A\|_2 \|A^{-1}\|_2 = \frac{\sigma_{\max}(A)}{\sigma_{\min}(A)}, \qquad \sigma_{\min}(A) > 0. \tag{8.11}$$

Table 3 reports the values for these specified matrices with $\mu = 1$ and $T = 0.9$.

Table 3. Spectral condition numbers of the explicitly specified product-integration and piecewise-constant Galerkin matrices at $T = 0.9$ with $\mu = 1$.

	Nyström-type method			Piecewise-constant Galerkin		
n	C, $p = 0.01$	C, $p = 0.4$	Elliptic	C, $p = 0.01$	C, $p = 0.4$	Elliptic
10	1.081007	1.206074	1.271273	1.081031	1.212243	1.294187
20	1.081055	1.215530	1.294283	1.081068	1.219379	1.314206
40	1.081080	1.221107	1.312954	1.081086	1.223477	1.330452
80	1.081092	1.224472	1.328659	1.081095	1.225926	1.344131

The condition numbers in this diagnostic are modest for all tested resolutions. They quantify the sensitivity of the stated discrete linear systems to algebraic perturbations, but do not by themselves

establish the accuracy of the continuous numerical approximation. This comparison is intended as an independent numerical validation for the present smooth test problem and does not imply the same convergence rate for nonsmooth solutions.

Case (4): Numerical investigation of the general hypergeometric kernel

From the numerical results obtained from the general hypergeometric kernel, the computed solution for the parameter pair $(p, q) = \left(\frac{1}{6}, \frac{3}{2}\right)$ remains close to the prescribed free function when the time-dependent coefficient is small. This behavior indicates a limited contribution of the integral operator under the considered numerical conditions, rather than an established state of physical stabilization. The computed solution exhibits increasing deviations from the free function as the time coefficient increases.

Regarding the behavior of the time coefficient at $(p, q) = \left(\frac{1}{6}, \frac{3}{2}\right)$ and time $t = 0.01$, we find that the computed solution is nearly identical to the prescribed free function. This reflects the very small contribution of the time-dependent integral term at this early time, without implying a particular physical interaction mechanism.

It is interesting to note that the behavior of the integral operator and the effect of the time coefficient on it at small time scales, for the selected admissible parameter pairs $(p, q) = \left(\frac{1}{6}, \frac{3}{2}\right)$ and $(p, q) = (0.4, 2)$, indicate that the numerical solutions remain close to the free function when the contribution of the integral term is small.

At the intermediate time $t = 0.4$, the numerical results for both selected parameter pairs illustrate the influence of the increasing time-dependent coefficient on the computed solutions. The deviation from the free function becomes more noticeable as this coefficient increases, without implying a state of physical or mathematical equilibrium.

Figure 9 shows the numerical solution for $(p, q) = (1/6, 3/2)$.

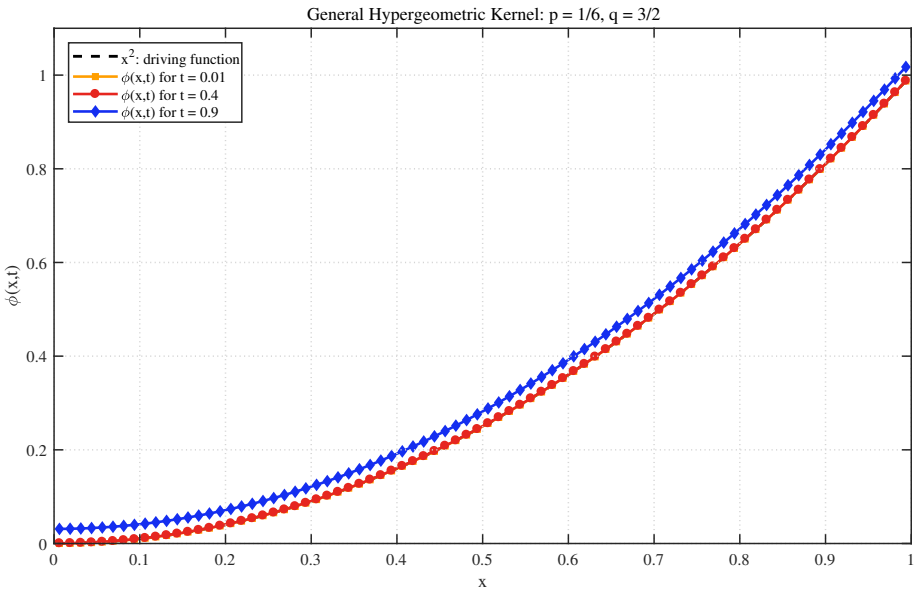


Figure 9. The numerical solution for the general hypergeometric kernel at different times for $(p, q) = \left(\frac{1}{6}, \frac{3}{2}\right)$. The curves represent $\phi(x, t)$ for $t = 0.01, 0.4, 0.9$, with $\mu = 1$ and $n = 80$.

Figure 10 shows the corresponding estimated mesh-refinement differences.

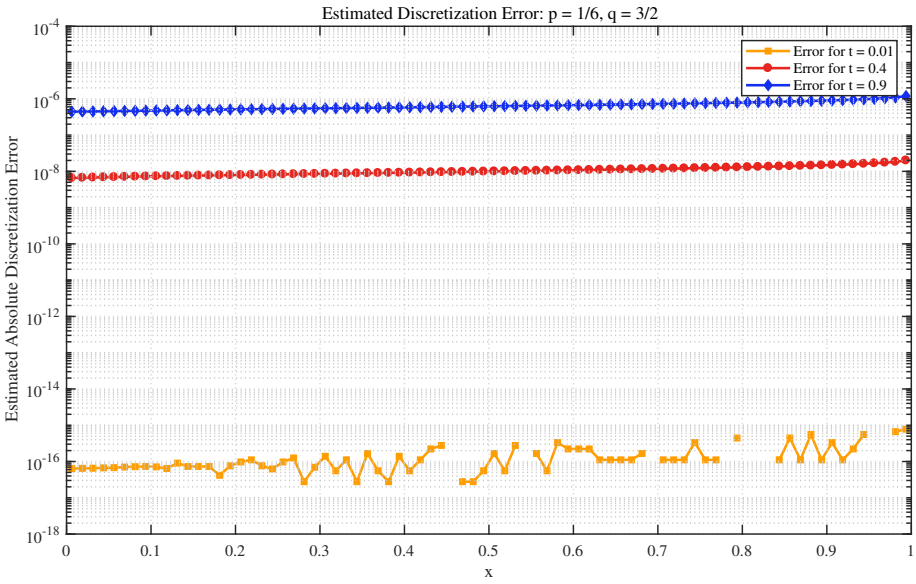


Figure 10. The estimated discretization error for the general hypergeometric kernel at different times for $(p, q) = \left(\frac{1}{6}, \frac{3}{2}\right)$. For $\mu = 1$ and $t = 0.01, 0.4, 0.9$, the plotted mesh-refinement difference is $E_{80,160}(x_i, t) = |\phi_{80}(x_i, t) - \phi^{\text{ext}}_{160}(x_i, t)|$, where the refined solution is evaluated at the coarse-grid nodes. The vertical scale is logarithmic.

Figure 11 shows the numerical solution for $(p, q) = (0.4, 2)$.

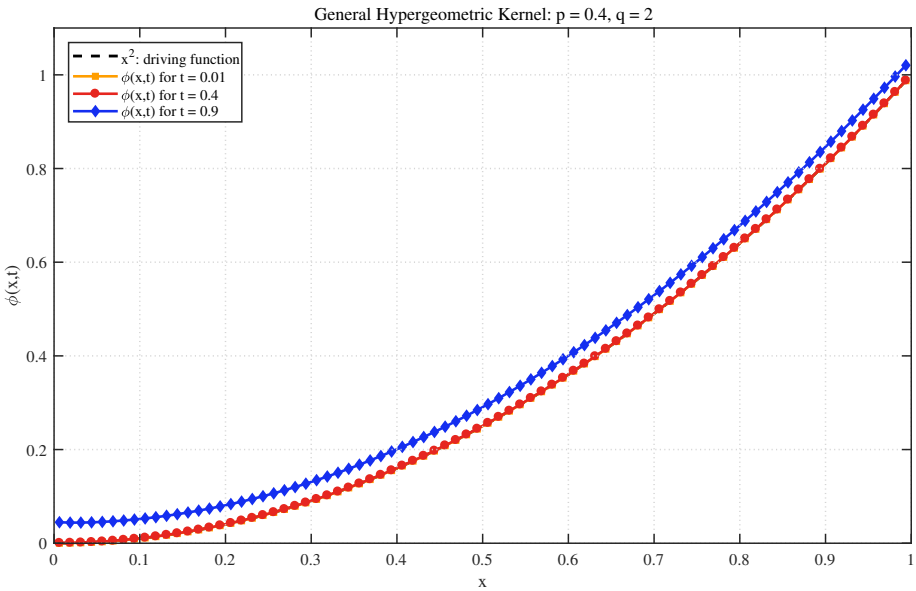


Figure 11. The numerical solution for the general hypergeometric kernel at different times for $(p, q) = (0.4, 2)$. The curves represent $\phi(x, t)$ for $t = 0.01, 0.4, 0.9$, with $\mu = 1$ and $n = 80$.

Figure 12 shows the corresponding estimated mesh-refinement differences.

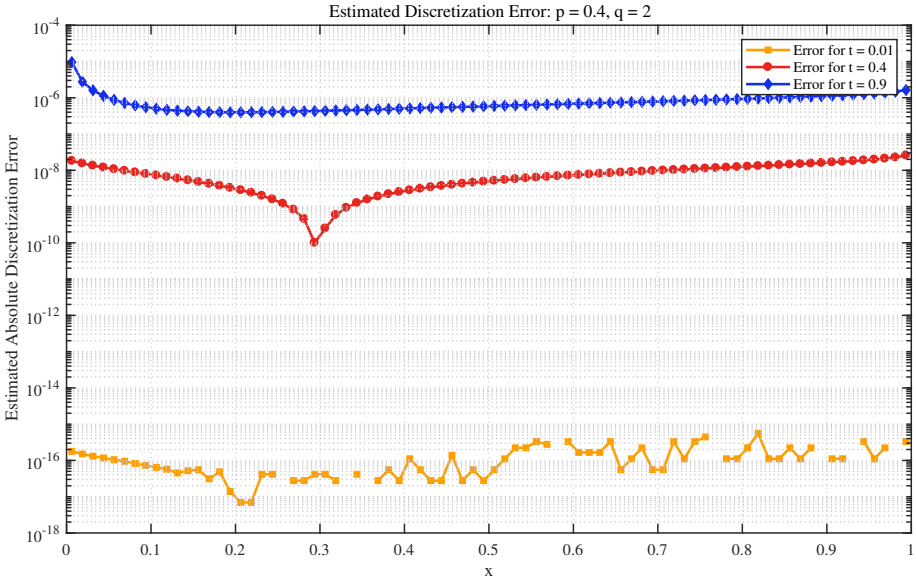


Figure 12. The estimated discretization error for the general hypergeometric kernel at different times for $(p, q) = (0.4, 2)$. For $\mu = 1$ and $t = 0.01, 0.4, 0.9$, the plotted mesh-refinement difference is $E_{80,160}(x_i, t) = |\phi_{80}(x_i, t) - \phi^{\text{ext}}_{160}(x_i, t)|$, where the refined solution is evaluated at the coarse-grid nodes. The vertical scale is logarithmic.

At time $t = 0.9$ and for the parameter pair $(p, q) = \left(\frac{1}{6}, \frac{3}{2}\right)$, the contribution of the spatial integral operator becomes more noticeable as the time-dependent coefficient increases. At this stage, the numerical solution shows a clearer deviation from the free function, with a maximum deviation of approximately 3.22×10^{-2}.

We should also note that, at high time values, the effect of the parameter choice becomes more pronounced. For the parameter pair $(p, q) = (0.4, 2)$, the corresponding deviation from the free function is stronger, reaching approximately 4.48×10^{-2} at $t = 0.9$.

As can be seen from the estimated error curves for the two cases $(p, q) = \left(\frac{1}{6}, \frac{3}{2}\right)$ and $(p, q) = (0.4, 2)$, the estimated discretization error increases as time increases. At $t = 0.9$, the maximum estimated error is approximately 1.19×10^{-6} for the first case and 9.59×10^{-6} for the second case. These values represent differences between the $n = 80$ and $n_{\text{ref}} = 160$ solutions, not errors against an exact solution. At $t = 0.01$, the differences are close to floating-point roundoff. The second parameter pair produces a somewhat larger numerical response and mesh-refinement difference under the stated conditions.

9. Conclusions

In this paper, we considered a mixed integral equation of the second kind with a hypergeometric kernel in position and time. The main purpose was to clarify the mathematical role of the time-dependent coefficient in the integral operator, while considering possible physical interpretations only as illustrative analogies. The hypergeometric kernel was proved to give rise to several important special kernels, such as the logarithmic kernel, Carleman kernel, complete elliptic kernel, and other related special cases. These cases provide a unifying framework for describing various types of singular and nonlocal interactions.

Existence and uniqueness of the solution are proved under some boundedness and contraction conditions. In particular, the condition $BM_G < \mu$ guarantees that the corresponding fixed-point operator is contractive in the considered function space. It was also shown that the successive approximation scheme converges and the corresponding error equation has the same integral structure as the original problem. This shows the stability of the mathematical formulation under the given assumptions.

Using the adopted representation based on the separation of variables, the original mixed integral equation was reduced to a Fredholm integral equation with a time-dependent coefficient $\lambda(t)$. This reduction allows us to study the influence of time on the spatial integral operator. The numerical results show that at a very early time $t = 0.01$, the time coefficient becomes very small and the integral operator has almost no effect on the solution. The computed solution is thus nearly identical to the prescribed free function. At the intermediate time $t = 0.4$ the effect of the integral term starts to show and the solution starts to deviate slightly from the free function. At the later time $t = 0.9$ the time-dependent coefficient has a larger effect, and the deviation from the free function is more pronounced.

The singular behavior of the log kernel requires a careful numerical treatment and an appropriate spatial discretization. For the Carleman kernel, the fractional parameter p governs the strength of the singularity, and numerical results for $p = 0.01$ and $p = 0.4$ show an increasing effect of the integral term as p and the time-dependent coefficient increase. For the complete elliptic kernel, the computed solutions exhibit smooth spatial profiles in the reported examples, with a more pronounced deviation from the free function as the time-dependent coefficient increases. The numerical results for the general hypergeometric kernel demonstrate the influence of the chosen kernel parameters on the response of the integral system.

The existence and uniqueness proof, successive-approximation estimates, and perturbation bounds follow standard contraction arguments and serve as supporting analysis rather than independent methodological advances. The specific contribution is the comparative treatment of the logarithmic, Carleman, and complete elliptic specializations of a common hypergeometric spatial kernel, together with an examination of the corresponding separated spatial equations under the same prescribed time-dependent coefficient.

In summary, the numerical results illustrate how the time-dependent coefficient, the singularity strength of the kernel, and the spatial discretization affect the numerical behavior of the solution. Hence, the proposed formulation offers a convenient mathematical framework for the study of time-dependent mixed integral equations with hypergeometric kernels and their special cases.

These numerical observations concern the prescribed mathematical model and do not independently establish physical phenomena such as energy accumulation, equilibrium, or stabilization. A rigorous physical interpretation would require a derivation from governing physical equations, identification of the relevant parameters, and validation against physical data.

Author contributions

Jihan Alahmadi: Conceptualization, methodology, formal analysis, investigation, validation, writing – original draft, writing – review & editing; M. A. Abdou: Conceptualization, methodology, formal analysis, investigation, validation, writing – original draft, writing – review & editing; M. Mahmoud Ismail: Conceptualization, methodology, formal analysis, investigation, validation, writing – original draft, writing – review & editing. All authors have read and approved the final version of the

manuscript for publication.

Use of Generative-AI tools declaration

ChatGPT was used to support manuscript revision, including language editing and comparison with previous studies. All authors reviewed the final manuscript and take full responsibility for its content.

Conflict of interest

The authors declare that they have no competing interests.

References

1. M. Lienert, R. Tumulka, A new class of Volterra-type integral equations from relativistic quantum physics, *J. Integral Equ. Appl.*, **31** (2019), 535–569. https://doi.org/10.1216/JIE-2019-31-4-535
2. K. Ata, M. Sahin, An integral equation approach for the solution of the Stokes flow with Hermite surfaces, *Eng. Anal. Bound. Elem.*, **96** (2018), 14–22. https://doi.org/10.1016/j.enganabound.2018.07.017
3. J. Gao, M. Condon, A. Iserles, Spectral computation of highly oscillatory integral equations in laser theory, *J. Comput. Phys.*, **395** (2019), 351–381. https://doi.org/10.1016/j.jcp.2019.06.045
4. R. T. Matoog, Treatments of probability potential function for nuclear integral equation, *J. Phys. Math.*, **8** (2017), 226. https://doi.org/10.4172/2090-0902.1000226
5. A. R. Jan, An asymptotic model for solving mixed integral equation in position and time, *J. Math.*, **2022** (2022), 8063971. https://doi.org/10.1155/2022/8063971
6. A. A. Sharif, A. A. Hamoud, K. P. Ghadle, Solving nonlinear integro-differential equations by using numerical techniques, *Acta Univ. Apulensis*, **61** (2020), 45–53.
7. A. R. Jan, Numerical solution via a singular mixed integral equation in (2 + 1) dimensional, *Appl. Math. Inf. Sci.*, **16** (2022), 871–882. https://doi.org/10.18576/amis/160603
8. M. A. Abdou, A. A. Soliman, M. A. Abdel-Aty, On a discussion of Volterra–Fredholm integral equation with discontinuous kernel, *J. Egypt. Math. Soc.*, **28** (2020), 11. https://doi.org/10.1186/s42787-020-00074-8
9. A. R. Jan, Solution of nonlinear mixed integral equation via collocation method basing on orthogonal polynomials, *Heliyon*, **8** (2022), e11827. https://doi.org/10.1016/j.heliyon.2022.e11827
10. G. A. Mosa, M. A. Abdou, A. S. Rahby, Numerical solutions for nonlinear Volterra–Fredholm integral equations of the second kind with a phase lag, *AIMS Mathematics*, **6** (2021), 8525–8543. https://doi.org/10.3934/math.2021495
11. H. X. Mamatova, Z. K. Eshkuvatov, Sh. Ismail, A hybrid method for all types of solutions of the system of Cauchy-type singular integral equations of the first kind, *Mathematics*, **11** (2023), 4404. https://doi.org/10.3390/math11204404

12. B. Sahu, A. Setia, M. T. Nair, A. Yadav, A numerical solution to the system of Cauchy singular integral equations with unbounded endpoint conditions, *Math. Comput. Simul.*, **248** (2026), 26–41. https://doi.org/10.1016/j.matcom.2026.04.002
13. R. Kress, *Linear integral equations*, 3 Eds., New York: Springer, 2014. https://doi.org/10.1007/978-1-4614-9593-2
14. K. E. Atkinson, *The numerical solution of integral equations of the second kind*, Cambridge: Cambridge University Press, 1997. https://doi.org/10.1017/CBO9780511626340
15. L. N. Trefethen, *Approximation theory and approximation practice*, Philadelphia: Society for Industrial and Applied Mathematics (SIAM), 2013. https://doi.org/10.1137/1.9781611975949
16. A. R. Jan, Phase-lag mixed integral equation of a generalized symmetric potential kernel and its physical meanings in (3 + 1) dimensions, *Heliyon*, **11** (2025), e42316. https://doi.org/10.1016/j.heliyon.2025.e42316
17. O. Nave, Modification of semi-analytical method applied system of ODE, *Mod. Appl. Sci.*, **14** (2020), 75–81. https://doi.org/10.5539/mas.v14n6p75
18. A. M. S. Mahdy, D. Sh. Mohamed, Approximate solution of Cauchy integral equations by using Lucas polynomials, *Comput. Appl. Math.*, **41** (2022), 403. https://doi.org/10.1007/s40314-022-02116-6
19. S. M. Mkhitarian, M. A. Abdou, On different methods for solving Fredholm integral equations of the first kind with logarithmic kernel, *Dokl. Akad. Nauk Armenii*, **90** (1989), 1–10.
20. S. M. Mkhitarian, M. A. Abdou, On different methods for solving Fredholm integral equations of the first kind with Carleman kernel, *Dokl. Akad. Nauk Armenii*, **90** (1989), 125–130.
21. *NIST digital library of mathematical functions*, National Institute of Standards and Technology, Chapters 15 and 19. Available from: `https://dlmf.nist.gov/`.



AIMS Press

© 2026 the Author(s), licensee AIMS Press. This is an open access article distributed under the terms of the Creative Commons Attribution License (https://creativecommons.org/licenses/by/4.0)